Two-Dimensional Carbon-Coated Graphene/Metal Oxide Hybrids for Enhanced Lithium Storage

Yuezeng Su,[†,§] Shuang Li,[†,§] Dongqing Wu,[‡,*] Fan Zhang,[‡] Haiwei Liang,[‡] Pengfei Gao,[‡] Chong Cheng,[‡] and Xinliang Feng[‡,#,*]

[†]School of Aeronautics and Astronautics, [‡]School of Chemistry and Chemical Engineering, Shanghai Jiao Tong University, Dongchuan Road 800, 200240, Shanghai, P. R. China and [#]Max Planck Institute for Polymer Research, Ackermannweg 10, 55128, Mainz, Germany. [§]These two authors contributed equally to this work.

ABSTRACT

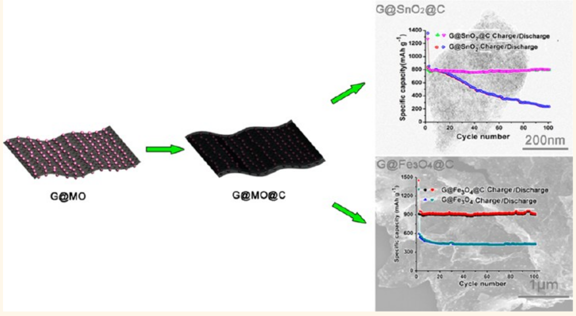

Metal oxides (MOs) have been widely investigated as promising high-capacity anode material for lithium ion batteries, but they usually exhibit poor cycling stability and rate performance due to the huge volume change induced by the alloying reaction with lithium. In this article, we present a double protection strategy by fabricating a two-dimensional (2D) core—shell nanostructure to improve the electrochemical performance of metal oxides in lithium storage. The 2D core—shell architecture is constructed by confining the well-defined graphene based metal oxides nanosheets (G@MO) within carbon layers. The resulting 2D carbon-coated graphene/metal oxides nanosheets (G@MO@C) inherit the advantages of graphene, which possesses high electrical conductivity, large aspect ratio, and thin feature. Furthermore, the carbon shells can tackle the deformation of MO nanoparticles while keeping the overall electrode highly conductive and active in lithium storage. As the result, the produced G@MO@C hybrids exhibit outstanding reversible capacity and excellent rate performance for lithium storage (G@SnO_2@C, 800 mAh g^{-1} at the rate of 200 mA g^{-1} after 100 cycles; G@Fe_3O_4@C, 920 mAh g^{-1} at the rate of 200 mA g^{-1} after 100 cycles).

KEYWORDS: lithium-ion battery · metal oxide · 2D nanosheet · graphene · core—shell

Lithium-ion batteries (LIBs) have been considered as the most effective and practical technologies for electrochemical energy storage.[1] To meet the demand for LIBs with high energy density and excellent cycle performance, numerous efforts have been devoted to the development of new electrode materials.[2−6] Electrochemically active metal oxides (MOs) such as SnO_2,[7,8] TiO_2,[9] Co_3O_4,[10,11] Mn_3O_4,[12] Fe_3O_4,[13] and Fe_2O_3[14] have emerged as the most promising candidates for the anode materials in the next-generation LIBs due to their high theoretical capacities and natural abundance. However, the extremely high volume change induced by the alloying reaction with lithium is the bottleneck for the commercialization of these materials. The so-called pulverization problem can cause a breakdown in electrical contact pathways between MOs, leading to rapid capacity fading during charge−discharge cycling.[15,16] To overcome these obstacles, carbonaceous materials are commonly introduced as matrices to absorb the volume changes and improve the structural stability of the electrodes.[17,18]

Graphene, a honeycomb network of sp^2 carbon atoms, has become one of the most appealing carbon matrices due to its outstanding electrical conductivity, excellent mechanical flexibility, large specific surface area,[10] and high thermal and chemical stability.[19−21] Consequently, various graphene-based metal oxide (G@MO) hybrids, have been developed for lithium storage. With respect to graphite,[1] carbon black,[22] and carbon nanotubes,[17,23] graphene exhibits the advantages of maintaining high electrical conductivity of the overall electrode and effective buffering of the strain from the volume change of MOs during the cycling processes.[24−26] Nevertheless, the exposed MO nanoparticles on the graphene surface are still prone to disintegrate or break down and, meanwhile, the volume expansion and aggregation of these active nanoparticles are difficult to avoid.[27,28] These handicaps can lead to a decreased electrochemical performance of G@MO hybrids. Therefore, it is highly desirable to develop G@MO hybrids with unique structures that can tackle the aggregation of nanoparticles

* Address correspondence to
wudongqing@sjtu.edu.cn,
feng@mpip-mainz.mpg.de.

Received for review July 11, 2012
and accepted August 29, 2012.

10.1021/nn303091t

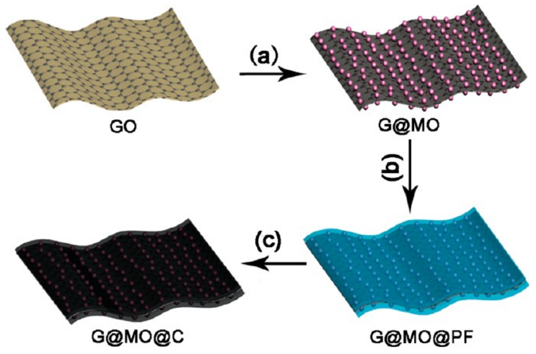

Scheme 1. Schematic illustration of synthesis of 2D core–shell G@MO@C hybrids: (a) hydrolysis of metal salt on GO; (b) *in-situ* polymerization of PF on G@MO; (c) carbonization of PF.

while keeping the overall electrode highly conductive and active in lithium storage.[9−13]

In this work, we present an unprecedented strategy to fabricate 2D G@MO nanosheets confined within a carbon layer (G@MO@C). The overall synthetic procedure of G@MO@C is illustrated in Scheme 1. First, 2D G@MO nanosheets were synthesized *via* an *in situ* hydrolysis of corresponding metal salt on the poly(dimethyldiallyl ammonium) chloride (PDDA) functionalized graphene oxide (GO). Next, *in situ* polymerization of phenol and formaldehyde in the presence of G@MO generated a phenol-formaldehyde (PF) resol encapsulated product, namely G@MO@PF. Finally, thermal treatment of G@MO@PF at 500 °C in N_2 led to the formation of a carbon shell coated over G@MO. By this means, monodisperse 2D core–shell hybrids, such as G@SnO_2@C and G@Fe_3O_4@C, could be fabricated, indicating the general applicability of our synthetic protocol. The formed 2D core–shell hybrids inherit the features from graphene[13] that possesses high electrical conductivity, large aspect ratio, and negligible thickness. As a consequence, the obtained G@MO@C manifests superior reversible capacity, cycle performance, and rate performance compared with bare G@MO. Moreover, owing to the efficient protection of the carbon shells, G@MO@C even exhibits much higher cycling stability than the other recently reported graphene-based MO composites, which generally suffer from the exfoliation of MO particles and rapid fading capacity after the first decades of cycles.[29−32]

RESULTS AND DISCUSSION

The morphology and structure of the resultant G@SnO_2, G@SnO_2@PF, and G@SnO_2@C were examined by field emission scanning electron microscope (FE-SEM), transition electron microscope (TEM), and atomic force microscope (AFM) measurements. SEM image of G@SnO_2 reveals that SnO_2 nanoparticles are uniformly deposited on graphene to form 2D sandwich-like architecture (Figure 1a). After the introduction of an additional PF layer, SEM (Figure 1b) and TEM (Figure 1c) characterizations show that the 2D morphology can be well maintained for G@SnO_2@PF. AFM study further suggests a thickness of about 12 and 20 nm for G@SnO_2 and G@SnO_2@PF, respectively (Figure 1e,f). It is noted that G@SnO_2@PF displays a smoother surface than G@SnO_2. These results thus unambiguously validate that an additional polymer layer has been successfully introduced with a thickness of about 4 nm on each side of G@SnO_2. Upon thermal treatment at 500 °C, SnO_2 nanoparticles remain homogeneously distributed in G@SnO_2@C (Figure 1d). TEM images of G@SnO_2@C (Figure 2a) clearly show that the SnO_2 nanoparticles feature a size of 3–5 nm and are fully imbedded in the carbon shell. The lattice fringe orientations in the high-resolution TEM (HRTEM) image (Figure 2b) demonstrate clear shell lattice fringes with *d*-spacings of 0.33 nm, corresponding to the (110) planes of rutile phase SnO_2. Furthermore, as unraveled by the elemental mapping of G@SnO_2@C for C, Sn, and O (Figure 2c), the homogeneous distribution of SnO_2 nanoparticles in these nanocomposites can be reserved after the coating of carbon layers.

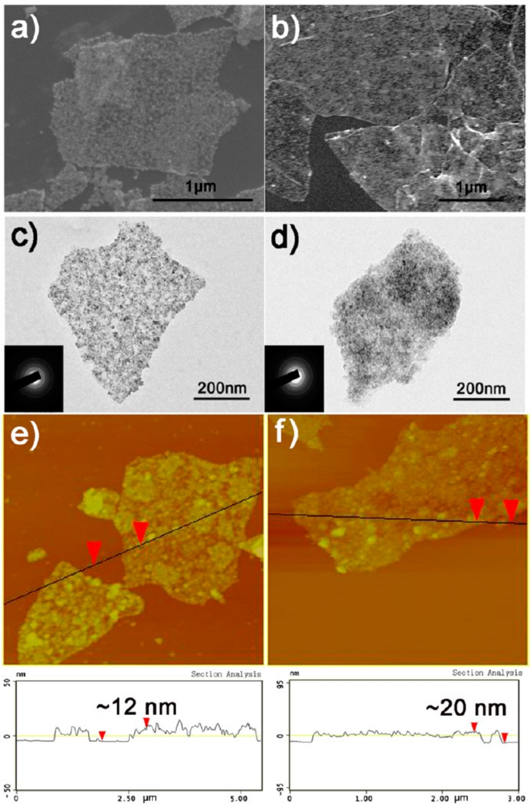

Figure 1. SEM images of (a) G@SnO_2 and (b) G@SnO_2@PF; TEM images of (c) G@SnO_2@PF and (d) G@SnO_2@C; AFM images of (e) G@SnO_2 and (f) G@SnO_2@PF.

Next, a powder X-ray diffraction (XRD) experiment was carried out to gain insight into the internal structure of G@SnO_2 and G@SnO_2@C. Apparently, both hybrids exhibit similar patterns (Figure 3a), and all intensive peaks can be well indexed to rutile SnO_2 (JCPDS No. 41-1445), suggesting that the deposition of carbon layer has no obvious influence on the crystal structure of SnO_2. A small peak marked by asterisk (∗) in the case of G@SnO_2@C can be assigned to SnO (JCPDS No. 06-0395), ascribable to a tiny reduction of SnO_2 during thermal treatment.[29] Thermogravimetric analysis (TGA), carried out in air at a heating rate of 20 °C min^{-1}, was used to determine the chemical composition of the G@SnO_2@C composite (Figure 3c). The results showed that the G@SnO_2@C composite contains ~12 wt % carbon, which matches well with the result of element analysis (EA, Supporting Information). The obtained materials were further examined by Raman spectra (Figure 3b). The G band of G@SnO_2@C is distinctly sharper than that of G@SnO_2. Moreover, the intensity ratio of the G to D band is also higher for G@SnO_2@C than that of G@SnO_2, indicating a good graphitic crystallinity of carbon shell resultant from the pyrolysis of PF which consists of a large amount of aromatic units.[33]

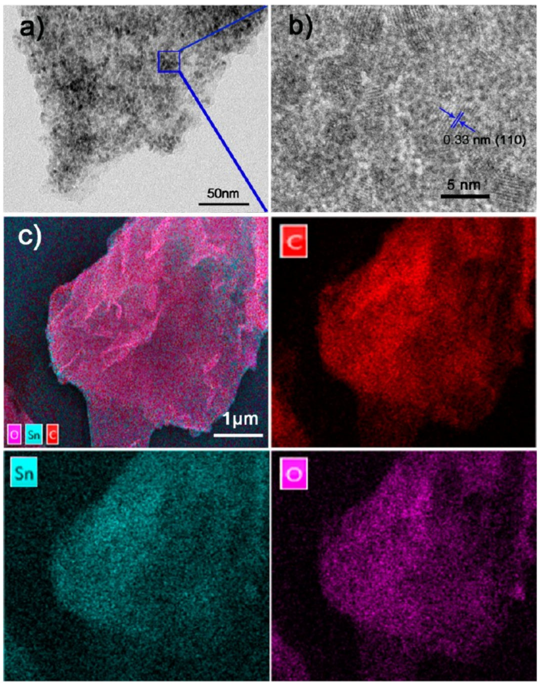

Figure 2. (a) TEM and (b) HRTEM images of G@SnO_2@C sheets. (c) Elemental mapping images of G@SnO_2@C sheets (by SEM): Carbon (C), tin (Sn), and oxygen (O) distribution in the selected area.

The electrochemical properties of G@SnO_2@C were then evaluated by galvanostatic charge/discharge cycling in a cell using lithium metal as the counter electrode between 0.01 and 3 V at a current density of 200 mAg^{-1}. The first discharge/charge step delivers a specific discharge capacity of 1270 mAh g^{-1} and charge capacity of 802 mAh g^{-1} with initial Coulombic efficiency of 62% (Figure 3d). This initial capacity loss can be possibly attributed to the formation of a solid electrolyte interphase (SEI) layer on the electrode surface during the first discharge step.[22] It is striking to note

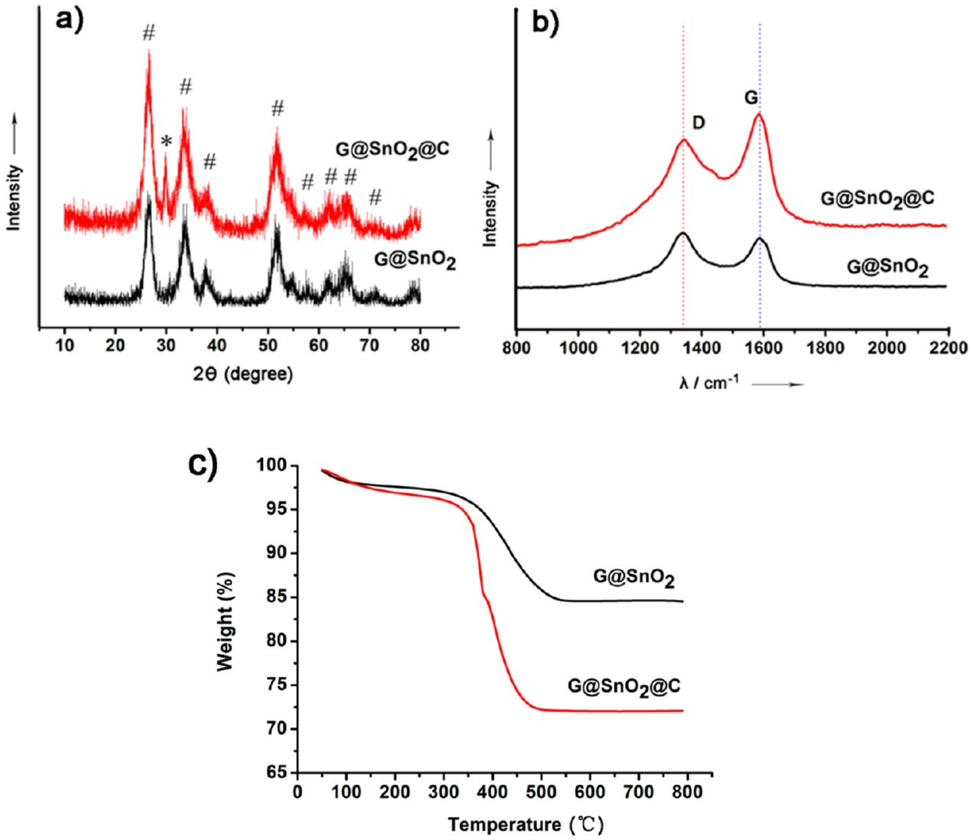

Figure 3. (a) XRD patterns, (b) Raman, and (c) TGA of G@SnO_2 and G@SnO_2@C hybrids.

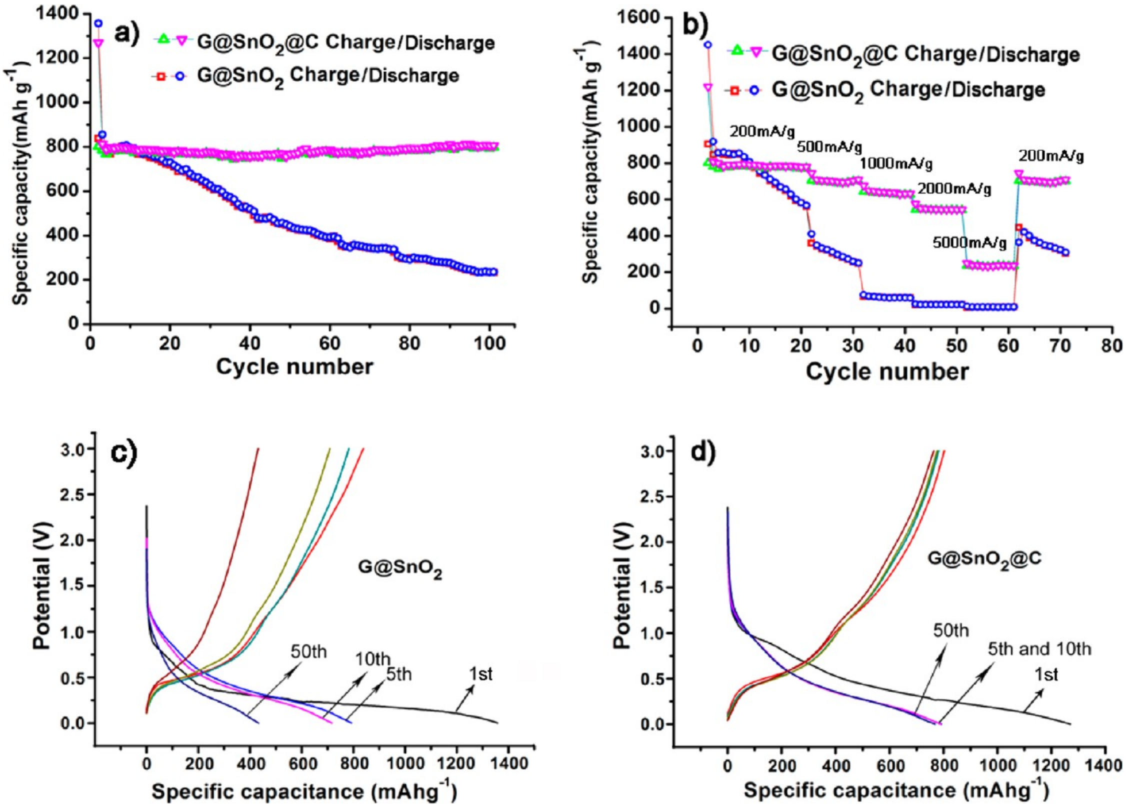

Figure 4. (a) Reversible charge/discharge capacities against cycle number for G@SnO_2 and G@SnO_2@C at a current density of 200 mA g^{-1} in the voltage window of 0.01−3.00 V; (b) rate performance of G@SnO_2 and G@SnO_2@C electrodes; (c) charge/discharge profiles of G@SnO_2, (d) G@SnO_2@C at a current density of 200 mA g^{-1} in a voltage window of 0.01−3.00 V: the discharge curves in the 1st, 5th, 10th, and 50th cycles.

that a reversible capacity up to 800 mAh g^{-1} could be maintained after 100 cycles without an apparent capacity loss (Figure 4a). This value is much higher than the theoretical specific capacity of the graphite electrode (372 mAh g^{-1}). For comparison, G@SnO_2 was also examined under the same electrochemical condition. Albeit with a higher weight content of SnO_2 for G@SnO_2 (according to the elemental analysis in Table S1, 90 wt %) than that of G@SnO_2@C (80 wt %), the specific capacity of G@SnO_2 decreased gradually from 800 mAh g^{-1} at the first 5e cycles to 235 mAh g^{-1} after 100 cycles (Figure 4a). The rate performance of G@SnO_2 and G@SnO_2@C electrodes was further inspected, as shown in Figure 4b. Remarkably, a high rate capacity up to 260 mAh g^{-1} for G@SnO_2@C at 5000 mA g^{-1} could be achieved. In contrast, the capacity of G@SnO_2 decreased promptly at each rate, dropping to 9 mAh g^{-1} at 5000 mA g^{-1}. To our best knowledge, such electrochemical performance of G@SnO_2@C is superior to the literature reported graphene and other carbon based SnO_2 nanocomposites.[17,18,27,34]

Our protocol can be further extended to the construction of 2D core−shell hybrids consisting of other electrochemically active metal oxides. For instance, the carbon-coated graphene-based Fe_3O_4 (G@Fe_3O_4@C) was also successfully fabricated. SEM images (Figure 5a) of G@Fe_3O_4@C reveal that the Fe_3O_4 particles are distributed homogeneously on the surface of graphene sheets. The resultant G@Fe_3O_4@C was further characterized by X-ray diffraction (Figure 5b). Notably, all the diffraction peaks of the G@Fe_3O_4@C can be perfectly indexed to the Fe_3O_4. The electrochemical performance of G@Fe_3O_4 and G@Fe_3O_4@C was also inspected. It is striking to note that a reversible capacity of about 920 mA h g^{-1} after 100 cycles can be achieved for G@Fe_3O_4@C, much higher than that of G@Fe_3O_4 (Figure 5c,d). Further, the rate performance of G@Fe_3O_4@C with a capacity of 550 mAh g^{-1} at 5000 mA g^{-1} also exceeds that of G@Fe_3O_4 (300 mAh g^{-1} at 5000 mA g^{-1}) and literature-reported Fe_3O_4-based nanocomposites.[35] It is interesting to note that the G@Fe_3O_4@C electrode shows distinct enhancement of the capacity retention in comparison with G@Fe_3O_4 electrode. This phenomenon could be attributed to the following reasons: First, all the Fe_3O_4 nanocrystals will contribute to the capacity since the carbon shell can effectively anchor the Fe_3O_4 nanoparticles on the surface of graphene. Second, the carbon shell of G@Fe_3O_4@C could improve the conductivity of the electrode, thus introduce fast electron and ion transport. Additionally, the conducting carbon layer can lead to the formation of uniform and thin SEI films on the surface of the composites to reduce the capacity loss at the first discharge/charge cycle.[36−39]

To gain insight into the prominent electrochemical behavior of G@MO@C with respect to the G@MO

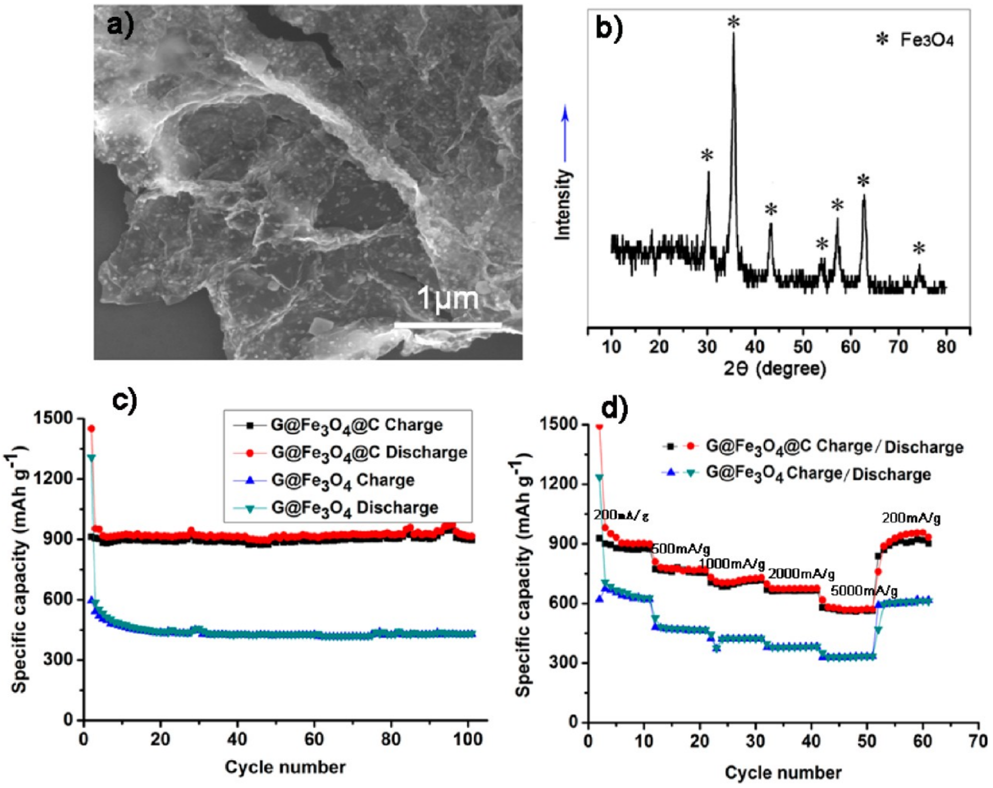

Figure 5. (a) SEM images and (b) XRD patterns of G@Fe_3O_4@C; (c) reversible charge/discharge capacities against cycle number for G@Fe_3O_4 and G@Fe_3O_4@C at a current density of 200 mA g^{-1} in the voltage window of 0.01−3.00 V; (d) rate performance of G@Fe_3O_4 and G@Fe_3O_4@C electrodes at the rate of 200, 500, 1000, 2000, and 5000 mA g^{-1}.

electrode, AC impedance measurements were performed. Nyquist plots (Figure 6a,b) show that the diameter of the semicircle for G@MO@C electrodes in the high−medium frequency region is much smaller than that of G@MO, suggesting that G@MO@C electrodes possess lower contact and charge-transfer impedances. This result also validates that the introduced carbon shells can improve the electrical conductivity of the overall electrode. The equivalent circuit model of the studied system is also shown in Figure 6c to represent the internal resistance of the test battery according to literature.[11,40] As shown in Figure 6, the high-frequency semicircle corresponds to the constant phase element of the SEI film (CPE1) and contact resistance (R_f), the semicircle in the medium-frequency region is assigned to the charge-transfer impedance (R_{ct}) and constant phase element of electrode/electrolyte interface (CPE2), and Z_W is associated with the Warburg impedance corresponding to the lithium-diffusion process. The kinetic difference between G@MO and G@MO@C were simulated by modeling AC impendence spectra based on the modified Randles equivalent circuit (Figure 6c). The fitted impedance parameters are listed in Table 1. It can be seen that the SEI film resistance R_f and charge-transfer resistance R_{ct} of the G@MO@C electrode are significantly lower than those of bare G@MO, which confirms that the carbon shell can preserve the high conductivity of the G@MO@C composite electrode and thus greatly enhance rapid electron transport during the electrochemical lithium insertion/extraction reaction, resulting in significant improvement of the electrochemical performances.

The evolution of the morphology and structure of G@SnO_2 and G@SnO_2@C composites during the charge/discharge processes were further investigated in this work. The TEM images of G@SnO_2 after 100 cycles (Supporting Information, Figure S5a,b) clearly show that the SnO_2 nanoparticles on a G@SnO_2 composite exhibit obvious pulverization and aggregation after 100 cycles. In contrast, SnO_2 particles on G@SnO_2@C with a carbon shell do not suffer from distinct morphological changes and maintain the uniform distribution on graphene sheets (Supporting Information, Figure S5c,d). Furthermore, according to the AC impedance data of G@SnO_2 and G@SnO_2@C composites after cycling, Nyquist plots (Supporting Information, Figure S5e,f) show that the diameter of the semicircle for the G@SnO_2 electrode after 100 cycles in the high-medium frequency region is much bigger than that for the electrode before cycling, suggesting the increased contact and charge-transfer resistances of G@SnO_2 electrodes, which is mainly caused by the pulverization and aggregation of SnO_2 particles. In contrast, the diameter of the semicircle for G@SnO_2@C electrodes after 100 cycles is even smaller than that for the electrode before cycling, indicating the increased electric conductivity

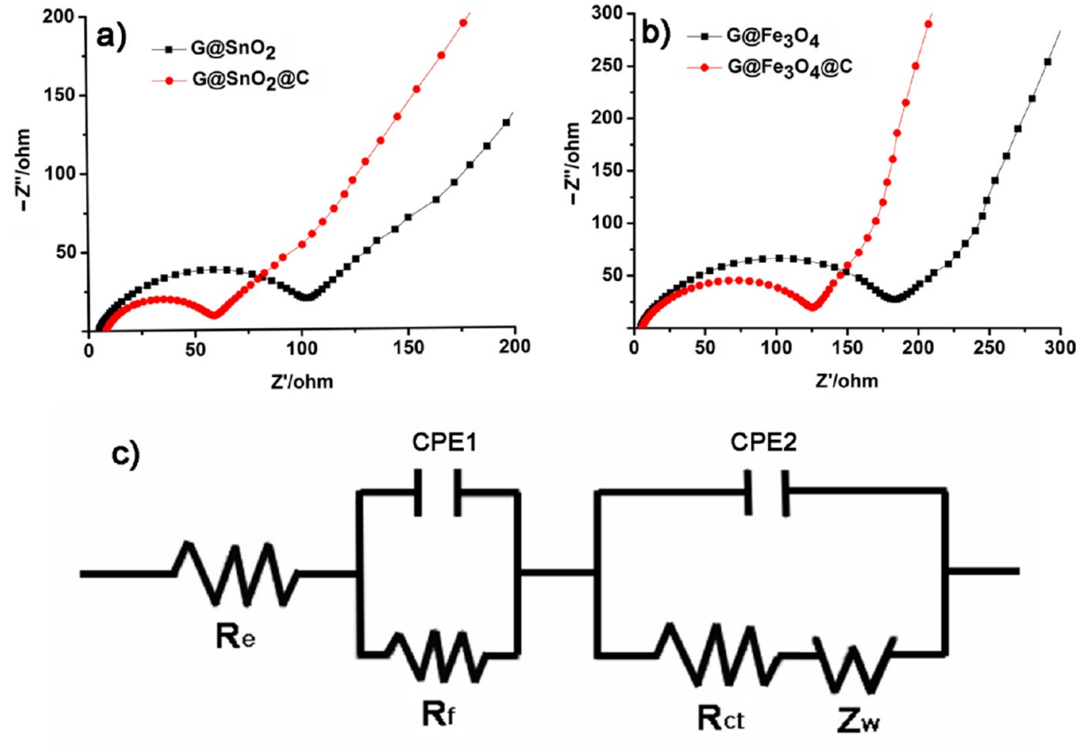

Figure 6. Nyquist plots of (a) G@SnO$_2$ and G@SnO$_2$@C electrodes and (b) G@Fe$_3$O$_4$ and G@Fe$_3$O$_4$@C obtained by applying a sine wave with amplitude of 5.0 mV over the frequency range 100 kHz−0.01 Hz. (c) Randles equivalent circuit for G@MO and G@MO@C electrode/electrolyte interface. R_e is the electrolyte resistance and R_f is the resistance of the surface film formed on the electrodes. R_{ct} is charge-transfer resistance, Z_w is the Warburg impedance related to the diffusion of lithium ions into the bulk electrodes and CPE represents the constant phase element, $Z_{CPE} = \{Q(j\omega)n\}^{-1}$, $0 \le n \le 1$.

TABLE 1. Kinetic Parameters of G@MO and G@MO@C Electrodes

samples	G@SnO$_2$	G@SnO$_2$@C	G@Fe$_3$O$_4$	G@Fe$_3$O$_4$@C
R_f (Ω)	107.3	54.4	189.2	129.5
R_{ct} (Ω)	87.7	53.2	168.4	117.2

resulting from the irreversible lithium insertion of the carbon shells with the growth of cycle number.[41] On the basis of the above results, the carbon shell not only provides effective protection of the MO nanoparticles on the surface of graphene but also improves the conductivity of the composites, which consequently enhances the electrochemical performance of G@MO@C composites.

Apparently, the superior electrochemical performance of G@MO@C for lithium storage can be assigned to the synergistic effects of graphene, MO, and the carbon layer associated with a unique 2D core−shell structure: (1) the nanoscale thickness of hybrids can efficiently reduce the diffusion length for both electrons and lithium ions; (2) the combination of graphene and carbon shell gives rise to a high electrical conductivity of the overall electrode and thus enhanced electron transport rate; (3) the coated carbon layers may improve the structural stability by suppressing the aggregation of MO nanoparticles and accommodate their volume expansion during the cycling.

CONCLUSION

In summary, we have developed a novel strategy to fabricate 2D core−shell G@MO@C hybrids. This enables an efficient encapsulation of electrochemically 2D graphene-based active metal oxide sheets by additional carbon layers, thus leading to an outstanding lithium storage performance including highly reversible capacity and excellent rate performance. We believe that the present synthetic protocol can be further extended to build up various 2D core−shell nanomaterials with promising applications in catalysis, sensing, supercapacitors, and fuel cells.

METHODS

Experimental Section. Graphene oxide (GO) was synthesized from natural graphite flakes by a modified Hummers method. Graphene-based SnO$_2$ nanosheets were prepared by *in situ* hydrolysis of Sn^{2+} on GO, using PDDA as the surfactant to assist the dispersibility of the formed G@SnO$_2$ hybrid: first, 60 mL of GO (0.50 mg/mL) and 1.2 mL of PDDA were mixed together, followed by ultrasonication for 15 min to form a homogeneous suspension. Subsequently, 0.45 mL of HCl (36 wt %) and 0.90 g of SnCl$_2$·2H$_2$O were added. The mixture was vigorously stirred at 90 °C for 1 h. Then, the resulting stable black suspension was centrifuged and washed with DI water for three times. Finally, the obtained G@SnO_2 was dispersed in 50 mL of DI water for further use.

G@SnO_2@C was prepared by *in situ* polymerization of phenol and formol in the presence of G@SnO_2 suspension. First, 300 mg of phenol and 70 mg of formol were dissolved in 20 mL of H_2O. This mixture was then added into 50 mL of G@SnO_2 suspension. Then, the mixture was heated to 90 °C in an oil bath. Afterward, 20 mL of 0.16 M NaOH solution was slowly added into the above mixture and kept at 90 °C overnight. The obtained materials were collected and washed with DI water for three times. Finally, the materials were dried in an oven at 60 °C for 12 h and then thermally treated at 500 °C in N_2 for 2 h. Regarding the use of glucose as the carbon source, G@SnO_2@$C_{glucose}$ sheets were synthesized through hydrothermal treatment of glucose in the presence of a G@SnO_2 suspension and following carbonization. First, 50 mL of G@SnO_2 suspension and glucose (with a different weight ratio to G@SnO_2 (25:1, 75:1, 150:1)) in 30 mL of DI water were added into 100 mL Teflon-lined stainless steel autoclaves for hydrothermal treatment at 180 °C for 12 h to produce glucose coated G@SnO_2@glucose. Then the obtained materials were treated at 500 °C in N_2 for 2 h to carbonize the coating layer.

The synthetic route of the G@Fe_3O_4@C hybrid is similar to that of G@SnO_2@C, only with modification of the employed precursors and reaction temperatures. Typically, for the synthesis of G@Fe_3O_4@C, 24 mg of $FeCl_3 \cdot 6H_2O$ and 380 mg of $FeCl_2 \cdot 4H_2O$ were first dissolved in 50 mL of H_2O and then added to 80 mL of GO/PDDA suspension and kept at 90 °C for 4 h. *In-situ* polymerization of PF and the following procedures were the same as those for the G@SnO_2@C composites.

Characterizations and Methods. SEM measurements were performed on a FEI Sirion-200 field emission scanning electron microscope. TEM studies were conducted on a JEOL-2100 electron microscope at an operating voltage of 200 kV. The sample was dissolved in water and the suspension was dropped onto a copper grid covered with carbon film. AFM images of the materials on a freshly cleaved mica surface were taken with a Nanoscope III in tapping mode using a NSC14/no Al probe (MikroMash, Wilsonville, Oregen). XRD analysis was performed on a Rigaku D/Max 2500 X-ray diffractometer with Cu Ka radiation (k = 1.54 Å) at a generator voltage of 40 kV and a generator current of 50 mA with a scanning speed of 5°/min from 10 to 80°. Raman measurements were recorded on an Invia/Reflrx Lasser Micro-Raman spectroscope (Renishaw, England) with excitation laser beam wavelength of 532 nm. The powders of G@SnO_2 and G@SnO_2@C were placed on a clean glass substrate that was used for the Raman measurement. Elemental analysis studies were tested on Vario EL III/Isoprime with G@SnO_2 and G@SnO_2@C powders.

Electrochemical Measurements. Electrochemical experiments were carried out in coin-type cells. The working electrodes were prepared by mixing the hybrids (G@SnO_2, G@SnO_2@C, G@Fe_3O_4, or G@Fe_3O_4@C), carbon black (Super-P), and poly(vinyl difluoride) (PVDF) at a weight ratio of 80:10:10 and pasting the mixture on pure copper foil (99.6%). Pure lithium foil was used as the counter-electrode. The electrolyte consisting of a solution of 1 M $LiPF_6$ in ethylene carbonate (EC)/dimethyl carbonate (DMC) (1:1 by volume) was obtained from Ube Industries Ltd. The cells were assembled in an argon-filled glovebox with the concentrations of moisture and oxygen below 1 ppm. The electrochemical performance was tested at various rates in the voltage range of 0.01−3.00 V.

Conflict of Interest: The authors declare no competing financial interest.

Acknowledgment. This work was financially supported by 973 Program of China (2012CB933404), Natural Science Foundation of China (21174083 and 21102091), BASF, Shanghai Pujiang Program (11PJ1405400), and the Ph.D. Programs Foundation of Ministry of Education of China for Young Scholars (20110073120039).

Supporting Information Available: Additional SEM, TEM, AFM, Raman, elemental analysis as well as electrochemical data. This material is available free of charge *via* the Internet at http://pubs.acs.org.

REFERENCES AND NOTES

1. Etacheri, V.; Marom, R.; Elazari, R.; Salitra, G.; Aurbach, D. Challenges in the Development of Advanced Li-Ion Batteries: A Review. *Energy Environ. Sci.* **2011**, *4*, 3243–3262.
2. Arico, A. S.; Bruce, P.; Scrosati, B.; Tarascon, J. M.; Van Schalkwijk, W. Nanostructured Materials for Advanced Energy Conversion and Storage Devices. *Nat. Mater.* **2005**, *4*, 366–377.
3. Idota, Y.; Kubota, T.; Matsufuji, A.; Maekawa, Y.; Miyasaka, T. Tin-Based Amorphous Oxide: A High-Capacity Lithium-Ion-Storage Material. *Science* **1997**, *276*, 1395–1397.
4. Maier, J. Nanoionics: Ion Transport and Electrochemical Storage in Confined Systems. *Nat. Mater.* **2005**, *4*, 805–815.
5. Lou, X. W.; Wang, Y.; Yuan, C.; Lee, J. Y.; Archer, L. A. Template-Free Synthesis of SnO_2 Hollow Nanostructures with High Lithium Storage Capacity. *Adv. Mater.* **2006**, *18*, 2325–2329.
6. Tarascon, J. M.; Armand, M. Issues and Challenges Facing Rechargeable Lithium Batteries. *Nature* **2001**, *414*, 359–367.
7. Wang, C.; Zhou, Y.; Ge, M.; Xu, X.; Zhang, Z.; Jiang, J. Z. Large-Scale Synthesis of SnO_2 Nanosheets with High Lithium Storage Capacity. *J. Am. Chem. Soc.* **2009**, *132*, 46–47.
8. Wang, Z.; Luan, D.; Boey, F. Y. C.; Lou, X. W. Fast Formation of SnO_2 Nanoboxes with Enhanced Lithium Storage Capability. *J. Am. Chem. Soc.* **2011**, *133*, 4738–4741.
9. Yang, S.; Feng, X.; Müllen, K. Sandwich-Like, Graphene-Based Titania Nanosheets with High Surface Area for Fast Lithium Storage. *Adv. Mater.* **2011**, *23*, 3575–3579.
10. Yang, S.; Feng, X.; Wang, L.; Tang, K.; Maier, J.; Müllen, K. Graphene-Based Nanosheets with a Sandwich Structure. *Angew. Chem., Int. Ed.* **2010**, *49*, 4795–4799.
11. Yang, S.; Feng, X.; Ivanovici, S.; Müllen, K. Fabrication of Graphene-Encapsulated Oxide Nanoparticles: Towards High-Performance Anode Materials for Lithium Storage. *Angew. Chem., Int. Ed.* **2010**, *49*, 8408–8411.
12. Wang, H.; Cui, L. F.; Yang, Y.; Sanchez Casalongue, H.; Robinson, J. T.; Liang, Y.; Cui, Y.; Dai, H. Mn_3O_4−Graphene Hybrid as a High-Capacity Anode Material for Lithium Ion Batteries. *J. Am. Chem. Soc.* **2010**, *132*, 13978–13980.
13. Qu, Q.; Yang, S.; Feng, X. 2D Sandwich-like Sheets of Iron Oxide Grown on Graphene as High Energy Anode Material for Supercapacitors. *Adv. Mater.* **2011**, *23*, 5574–5580.
14. Zhu, X. J.; Zhu, Y. W.; Murali, S.; Stoller, M. D.; Ruoff, R. S. Nanostructured Reduced Graphene Oxide/Fe_2O_3 Composite as a High-Performance Anode Material for Lithium Ion Batteries. *ACS Nano* **2011**, *5*, 3333–3338.
15. Huang, J. Y.; Zhong, L.; Wang, C. M.; Sullivan, J. P.; Xu, W.; Zhang, L. Q.; Mao, S. X.; Hudak, N. S.; Liu, X. H.; Subra-manian, A.; *et al.* *In-Situ* Observation of the Electrochemical Lithiation of a Single SnO_2 Nanowire Electrode. *Science* **2010**, *330*, 1515–1520.
16. Wang, C.-M.; Xu, W.; Liu, J.; Zhang, J.-G.; Saraf, L. V.; Arey, B. W.; Choi, D.; Yang, Z.-G.; Xiao, J.; Thevuthasan, S.; *et al.* *In-Situ* Transmission Electron Microscopy Observation of Microstructure and Phase Evolution in a SnO_2 Nanowire during Lithium Intercalation. *Nano Lett.* **2011**, *11*, 1874–1880.
17. Wang, Y.; Zeng, H. C.; Lee, J. Y. Highly Reversible Lithium Storage in Porous SnO_2 Nanotubes with Coaxially Grown Carbon Nanotube Overlayers. *Adv. Mater.* **2006**, *18*, 645–649.
18. Meduri, P.; Pendyala, C.; Kumar, V.; Sumanasekera, G. U.; Sunkara, M. K. Hybrid Tin Oxide Nanowires as Stable and High Capacity Anodes for Li-Ion Batteries. *Nano Lett.* **2009**, *9*, 612–616.
19. Fasolino, A.; Los, J. H.; Katsnelson, M. I. Intrinsic Ripples in Graphene. *Nat. Mater.* **2007**, *6*, 858–861.
20. Balandin, A. A.; Ghosh, S.; Bao, W.; Calizo, I.; Teweldebrhan, D.; Miao, F.; Lau, C. N. Superior Thermal Conductivity of Single-Layer Graphene. *Nano Lett.* **2008**, *8*, 902–907.
21. Geim, A. K.; Novoselov, K. S. The Rise of Graphene. *Nat. Mater.* **2007**, *6*, 183–191.

22. Yu, Y.; Chen, C. H.; Shi, Y. A Tin-Based Amorphous Oxide Composite with a Porous, Spherical, Multideck-Cage Morphology as a Highly Reversible Anode Material for Lithium-Ion Batteries. *Adv. Mater.* **2007**, *19*, 993–997.
23. Zhang, H. X.; Feng, C.; Zhai, Y. C.; Jiang, K. L.; Li, Q. Q.; Fan, S. S. Cross-Stacked Carbon Nanotube Sheets Uniformly Loaded with SnO_2 Nanoparticles: A Novel Binder-Free and High-Capacity Anode Material for Lithium-Ion Batteries. *Adv. Mater.* **2009**, *21*, 2299–2304.
24. Sun, Y. M.; Hu, X. L.; Luo, W.; Huang, Y. H. Self-Assembled Hierarchical MoO_2/Graphene Nanoarchitectures and Their Application as a High-Performance Anode Material for Lithium-Ion Batteries. *ACS Nano* **2011**, *5*, 7100–7107.
25. Wu, Z. S.; Ren, W. C.; Wen, L.; Gao, L. B.; Zhao, J. P.; Chen, Z. P.; Zhou, G. G.; Li, F.; Cheng, H. M. Graphene Anchored with Co_3O_4 Nanoparticles as Anode of Lithium Ion Batteries with Enhanced Reversible Capacity and Cyclic Performance. *ACS Nano* **2010**, *4*, 3187–3194.
26. Peng, C. X.; Chen, B. D.; Qin, Y.; Yang, S. H.; Li, C. Z.; Zuo, Y. H.; Liu, S. Y.; Yang, J. H. Facile Ultrasonic Synthesis of CoO Quantum Dot/Graphene Nanosheet Composites with High Lithium Storage Capacity. *ACS Nano* **2012**, *6*, 1074–1081.
27. Li, X.; Meng, X.; Liu, J.; Geng, D.; Zhang, Y.; Banis, M. N.; Li, Y.; Yang, J.; Li, R.; Sun, X.; *et al.* Tin Oxide with Controlled Morphology and Crystallinity by Atomic Layer Deposition onto Graphene Nanosheets for Enhanced Lithium Storage. *Adv. Funct. Mater.* **2012**, *22*, 1647–1654.
28. Park, M.-S.; Wang, G.-X.; Kang, Y.-M.; Wexler, D.; Dou, S.-X.; Liu, H.-K. Preparation and Electrochemical Properties of SnO_2 Nanowires for Application in Lithium-Ion Batteries. *Angew. Chem., Int. Ed.* **2007**, *46*, 750–753.
29. Lou, X. W.; Li, C. M.; Archer, L. A. Designed Synthesis of Coaxial SnO_2@carbon Hollow Nanospheres for Highly Reversible Lithium Storage. *Adv. Mater.* **2009**, *21*, 2536–2539.
30. Ding, S.; Chen, J. S.; Lou, X. W. One-Dimensional Hierarchical Structures Composed of Novel Metal Oxide Nanosheets on a Carbon Nanotube Backbone and Their Lithium-Storage Properties. *Adv. Funct. Mater.* **2011**, *21*, 4120–4125.
31. Paek, S.-M.; Yoo, E.; Honma, I. Enhanced Cyclic Performance and Lithium Storage Capacity of SnO_2/Graphene Nanoporous Electrodes with Three-Dimensionally Delaminated Flexible Structure. *Nano Lett.* **2008**, *9*, 72–75.
32. Zhang, W. M.; Hu, J. S.; Guo, Y. G.; Zheng, S. F.; Zhong, L. S.; Song, W. G.; Wan, L. J. Tin-Nanoparticles Encapsulated in Elastic Hollow Carbon Spheres for High-Performance Anode Material in Lithium-Ion Batteries. *Adv. Mater.* **2008**, *20*, 1160–1165.
33. Kishore, N.; Sachan, S.; Rai, K. N.; Kumar, A. Synthesis and Characterization of a Nanofiltration Carbon Membrane Derived from Phenol−Formaldehyde Resin. *Carbon* **2003**, *41*, 2961–2972.
34. Wang, D.; Kou, R.; Choi, D.; Yang, Z.; Nie, Z.; Li, J.; Saraf, L. V.; Hu, D.; Zhang, J.; Graff, G. L.; *et al.* Ternary Self-Assembly of Ordered Metal Oxide−Graphene Nanocomposites for Electrochemical Energy Storage. *ACS Nano* **2010**, *4*, 1587–1595.
35. Chen, W.; Li, S.; Chen, C.; Yan, L. Self-Assembly and Embedding of Nanoparticles by *in Situ* Reduced Graphene for Preparation of a 3D Graphene/Nanoparticle Aerogel. *Adv. Mater.* **2011**, *23*, 5679–5683.
36. Zhang, W. M.; Wu, X. L.; Hu, J. S.; Guo, Y. G.; Wan, L. J. Carbon Coated Fe_3O_4 Nanospindles as a Superior Anode Material for Lithium-Ion Batteries. *Adv. Funct. Mater.* **2008**, *18*, 3941–3946.
37. Li, B. J.; Cao, H. Q.; Shao, J.; Qu, M. Z. Enhanced Anode Performances of The Fe_3O_4-Carbon-rGO Three Dimensional Composite in Lithium Ion Batteries. *Chem. Commun.* **2011**, *47*, 10374–10376.
38. Li, B. J.; Cao, H. Q.; Shao, J.; Qu, M. Z.; Warnerc, J. H. Superparamagnetic Fe_3O_4 Nanocrystals@Graphene Composites for Energy Storage Devices. *J. Mater. Chem.* **2011**, *21*, 5069–5075.
39. Zhou, G. M.; Wang, D. W.; Li, F.; Zhang, L. L.; Li, N.; Wu, Z. S.; Wen, L.; Lu, G. Q.; Cheng, H. M. Graphene-Wrapped Fe_3O_4 Anode Material with Improved Reversible Capacity and Cyclic Stability for Lithium Ion Batteries. *Chem. Mater.* **2010**, *22*, 5306–5313.
40. Chang, K.; Chen, W. X. L-Cysteine-Assisted Synthesis of Layered MoS_2/Graphene Composites with Excellent Electrochemical Performances for Lithium Ion Batteries. *ACS Nano* **2011**, *28*, 4720–4728.
41. Giraudet, J.; Dubois, M.; Inacio, J.; Hamwi, A. Electrochemical Insertion of Lithium Ions into Disordered Carbons Derived from Reduced Graphite Fluoride. *Carbon* **2003**, *41*, 453–463.